Reliability-based Design Optimization for Lithium-ion Batteries Considering the Venting Critical Time

Tongguang Yang, Andong Ni, Zhiliang Huang, Hangyang Li, Huaixing Wang, Wanyi Tian, and Shouhua Yi

***Abstract*—Under thermal abuse conditions, lithium-ion batteries are subject to multiple sources of uncertainty, which can potentially trigger thermal runaway. To enable reliable structural design under thermal safety constraints, this study proposes a reliability-based design optimization (RBDO) method for lithium-ion batteries based on critical venting prediction. First, an analytical model is developed that couples electrochemical reactions, heat conduction, gas dynamics, and nonlinear elasticity, enabling a comprehensive characterization of the thermo-gas-mechanical evolution, with the critical venting time adopted as the performance metric. Second, global sensitivity analysis using a variance-based decomposition method identifies high-sensitivity parameters for dimensionality reduction. Finally, an RBDO model with venting response probability as the constraint is formulated, and an efficient solution strategy is established by integrating the performance measure approach with a decoupled optimization frame-work to ensure computational efficiency and numerical stability. Experimental results show that the proposed model achieves prediction errors lower than 3% for temperature and critical response. Compared to existing methods, it achieves a superior balance between accuracy and efficiency, with RBDO solution time under two hours. The proposed approach demonstrates strong engineering applicability and extensibility, offering an effective tool for safety-oriented structural optimization of lithium-ion batteries.**

***Index Terms*—Venting critical time, thermal abuse conditions, global sensitivity analysis, reliability-based design optimization (RBDO), lithium-ion batteries.**

NOMENCLATURE

A. Abbreviations

RBDO	reliability-based design optimization
RMSE	root mean square error
SEI	solid electrolyte interphase

B. Variables

Q	heat generation rate
t	current time
m_{A}	active material mass
h_{D}	enthalpy change of SEI decomposition
h_{R}	enthalpy change of regeneration reaction
v_{D}	reaction rate of SEI decomposition
v_{R}	reaction rate of regeneration reaction
f_{D}	reaction frequency of SEI decomposition
f_{R}	reaction frequency of regeneration reaction
E_{A}	activation energy
R_{U}	universal gas constant
x_{D}	fraction of lithium ions contained in the SEI
x_{D}^{0}	initial fraction of lithium ions contained in the SEI
x_{R}	fraction of lithium ions embedded in the SEI
x_{R}^{0}	initial fraction of lithium ions embedded in the SEI
y	dimensionless SEI thickness

Received: Febuary 11, 2025
Accepted: June 13, 2025
Published Online: November 1, 2025

Tongguang Yang (corresponding author), Zhiliang Huang, and Hangyang Li are with the Key Laboratory for Energy Monitoring and Edge Computing of Smart City, Hunan City University, Yiyang 413002, China (e-mail: yangtongguang1@163.com; 13787181710@163.com; lihangyang_cn@163.com).

Andong Ni is with the Key Laboratory for Energy Monitoring and Edge Computing of Smart City, Hunan City University, Yiyang 413002, China; and also with the School of Electrical Engineering, University of South China, Hengyang 421001, China (e-mail: 2712335793@qq.com).

Huaixing Wang is with the Huizhou Liwinon New Energy Technology Co., Ltd., Huizhou 516123, China (e-mail: huaixing_wang@163.com).

Wanyi Tian and Shouhua Yi are with the College of Mechanical and Vehicle Engineering, Hunan University, Changsha 410082, China (e-mail: tianwanyi2001@126.com; yishouhua @hnu.edu.cn).

DOI: 10.23919/PCMP.2025.000038

y^0	initial dimensionless SEI thickness
m_{G}	gas production amount
m_{G}^0	initial gas production amount
T_{A}	ambient temperature
A	heat transfer area
γ_{D}	gas production coefficient corresponding to the reaction of SEI decomposition
γ_{R}	gas production coefficient corresponding to the reaction of regeneration reaction
R_{G}	gap thermal resistance
K_{G}	thermal conductivity of the gas
δ	gap distance
δ^0	assembly gap
R_{A}	convective thermal resistance between the battery surface and the environment
h_{A}	heat transfer coefficient
C	thermal capacity of the battery
c	specific heat capacity
m_{B}	mass of the cell
P	gas pressure
R_{C}	gas constant
T	gas temperature
P_{A}	atmospheric pressure
E	elastic modulus in the mechanical constitutive equation
λ	strain exponent in the mechanical constitutive equation
H	dimensionless cell height
H^0	cell height
P_{thr}	pressure relief threshold
t_{C}	pressure relief critical time under thermal abuse conditions
$\boldsymbol{X}$	parameter vector containing 23 elements
$\boldsymbol{X}_j$	jth element of $\boldsymbol{X}$
$\boldsymbol{X}_j^{\mathrm{L}}$	lower boundary of the jth element of $\boldsymbol{X}$
$\boldsymbol{X}_j^{\mathrm{R}}$	upper boundary of the jth element of $\boldsymbol{X}$
$\boldsymbol{A}$	sample matrices
$\boldsymbol{B}$	sample matrices
$\boldsymbol{C}^{(j)}$	sample matrices
M	number of samples
$\boldsymbol{A}_i$	vector composed of the ith row elements of $\boldsymbol{A}$
$\boldsymbol{f}_{\boldsymbol{A}}$	response sample vectors
$\boldsymbol{f}_{\boldsymbol{B}}$	response sample vectors
$\boldsymbol{f}_{\boldsymbol{C}}^{(j)}$	response sample vectors
$\boldsymbol{V}_{\mathrm{f}}$	variance of the response samples
S_j^{T}	global sensitivity index
$\boldsymbol{Y}$	simplified by the parameter vector $\boldsymbol{X}$
$\boldsymbol{d}$	design vector
$\boldsymbol{d}^{\mathrm{L}}$	upper boundary of the design vector
$\boldsymbol{d}^{\mathrm{R}}$	lower boundary of the design vector
$t_{\mathrm{thr}}^{\mathrm{t}}$	target value for the venting critical time
P_{r}	probability of passing the thermal abuse test
P_{r}^t	target value of the probability of passing the thermal abuse test
$\boldsymbol{\mu}_{\boldsymbol{Y}}$	mean vector of $\boldsymbol{Y}$
$\boldsymbol{U}$	vector of $\boldsymbol{Y}$ in the standard normal space
β^{t}	target reliability index
$\boldsymbol{\Phi}^{-1}$	inverse function of the standard normal cumulative distribution
$\boldsymbol{Y}^*$	obtained maximum possible point is mapped back to the original space
$\boldsymbol{S}$	current shifting vector
$T_{\mathrm{A}}^{\max}$	cutoff temperature
μ_δ	nominal value of the assembly gap

I. Introduction

Due to their high energy density, long cycle life, and lack of memory, lithium-ion batteries have been the widely deployed in energy storage systems, electric vehicles, and portable electronic devices [1]. In recent years, emerging energy conversion technologies such as liquid-liquid interface-based triboelectric nanogenerators have also attracted attentions for microenergy harvesting in low-power applications [2]. However, for medium-power to high-power scenarios, lithium-ion batteries remain the most mature and technically advantageous solution. As deployment scales continue to grow, safety concerns during battery operation have become increasingly prominent, particularly the risk of thermal runaway under extreme operating conditions, which has emerged as a critical issue in current research. As the industry continues to enhance battery energy density, the safety of batteries during operation faces increasing challenges [3], particularly under thermal abuse conditions [4]. Under such conditions, the solid electrolyte interphase (SEI) on the anode decomposes, releasing heat and gas, thereby causing a rapid rise in the internal temperature and pressure of the battery. The increase in temperature further accelerates electrochemical reactions, creating a vicious cycle that can ultimately lead to thermal runaway of the battery cell [5]. In practical applications, multiple cells are assembled into high-energy-density battery packs through series

and parallel configurations. When one cell experiences thermal runaway, the heat released can quickly spread to adjacent cells, causing the runaway to propagate [6]. This can lead to catastrophic consequences, such as electric vehicle fires or energy storage station explosions [7], [8]. To reduce the risk of thermal runaway, lithium-ion batteries are equipped with an overpressure relief mechanism, which releases internal gases and electrolytes when the internal pressure exceeds a safety threshold, to prevent thermal runaway. However, activating this venting mechanism indicates a significant decline in battery performance and introduces potential safety risks, typically marking the end of the battery's lifespan [9]. Therefore, accurately predicting and effectively controlling the critical venting moment of lithium-ion batteries under thermal abuse conditions has become a key research focus.

Recently, researchers have developed a series of theories and methods to assess and manage the thermal behavior of lithium-ion batteries [10]. These studies are broadly categorized into two directions: state evolution assessment and design optimization. State evolution assessment involves the development of multi-physics simulation models that couples electrochemical reactions, heat transfer, and mechanics, to simulate the changes in temperature, pressure, and deformation of lithium-ion batteries during operation [11]. For example, Lee and Kim developed a bidirectional nonlinear mechanical-electrochemical-thermal coupling model to simulate the internal short circuit, voltage drop, and temperature rise of lithium-ion batteries under quasi-static indentation conditions. The predicted errors in short-circuit timing and peak temperature are lower than 4% [12]. In [13], a battery pack thermal runaway model is proposed that couples fluid dynamics and thermal resistance networks. This model simulates the temperature and gas concentration evolution in the porous structure during thermal runaway and reveals the influence of structural parameters on the propagation of thermal runaway. Reference [14] develops a coupled simulation model for cylindrical lithium-ion batteries, covering SEI decomposition, gas generation and combustion, solid particle ejection, and heat transfer. This model provides an effective tool for accurately predicting thermal runaway propagation. These studies, utilizing commercial finite element simulation software, enable high-fidelity state evolution analysis. However, their computational time typically takes hours, making them unsuitable for real-time applications.

To improve computational efficiency, researchers have attempted to construct coupled multi-physics analytical models [15]. These models generally use systems of ordinary differential equations to couple reaction kinetics, lumped heat transfer, and mechanical constitutive equations. They significantly reduce computational complexity while maintaining reasonable accuracy. For instance, a pseudo-three-dimensional multi-node electrothermal model is proposed for real-time prediction of the nonuniform temperature field evolution in large-sized prismatic batteries, with a temperature prediction error of less than 2.0 K [16]. A thermal runaway analytical model based on reaction kinetics and energy and mass conservation equations is developed, which clearly defines the quantitative relationship between the pressure threshold and thermal runaway timing [17]. In [18], a coupled electrochemical/thermal/mechanical analytical model is developed to assess the temperature and stress of prismatic batteries under high-temperature and rapid charge-discharge conditions, with temperature and stress errors of lower than 1% and 5%, respectively. These analytical models complete computations within seconds, offering both efficiency and acceptable accuracy, providing key technological support for online state monitoring and random response analysis of lithium-ion batteries. However, in practical applications, ensuring the robustness and convergence of these analytical models still presents challenges. In addition, several researchers have explored the use of electrochemical impedance spectroscopy data in combination with artificial intelligence techniques, such as transfer learning, to enhance state estimation capabilities. For instance, reference [19] proposes a hybrid health state estimation method that integrates an improved honey badger algorithm with a neural network architecture to predict the remaining useful life of supercapacitors, demonstrating the potential of intelligent algorithms in the lifetime modelling of electrochemical energy storage systems. Similarly, reference [20] develops a transfer learning-based approach for state-of-health estimation, which significantly improves the adaptability and generalization of EIS analysis across different types of lithium-ion batteries.

Design optimization uses state assessment models as performance functions. By constructing optimization models that include objectives and constraints, it explores optimized design solutions for lithium-ion batteries [21]. An electrochemical/thermal coupling model is utilized in [22] and it is revealed the influence of battery structural parameters and electrochemical properties on state responses through local sensitivity analysis, optimizing the battery design. In [23], an electrothermal model is developed for cylindrical lithium-ion batteries. By analyzing the impact of battery structure and cooling methods on temperature distribution, an optimization strategy is proposed to increase the number of tab connections and optimize side cooling. Reference [24] improves the temperature prediction accuracy of cylindrical batteries by optimizing the heat generation model and introducing correction factors, while an optimized cooling flow rate strategy for battery packs is also designed. However, most existing studies are based on deterministic design optimization, whereas the state evolution of lithium-ion batteries is significantly influenced by uncertainties, such as structural

dimensions, material properties, and operating parameters. Under the influence of these uncertainties, the battery state evolves randomly. Ignoring these effects may lead to design solutions with potential thermal runaway risks. Pioneering researches have emerged to address the impact of uncertainty on lithium-ion battery design. A thermal abuse safety risk assessment method is proposed for battery packs, which quantifies the effect of uncertainties on the probability of thermal runaway by embedding random models for battery parameters and loads [25]. In [26], an uncertainty-based design method is developed that considers manufacturing errors. This method optimizes the manufacturing cost of prismatic batteries while controlling fluctuations in their thermal performance. These studies not only maximize battery performance but also account for the impact of uncertainty, offering new solutions for the reliability design of battery structures.

In recent decades, reliability-based design optimization (RBDO) has developed into a widely applied theoretical framework [27], [28]. However, there are few reports on RBDO for lithium-ion batteries, mainly due to several unresolved technical challenges. First, there is a lack of uncertainty quantification frameworks with engineering applicability. State assessment of lithium-ion batteries typically involves dozens of input parameters. If large-scale sample data collection is performed for each parameter to construct a stochastic model, it inevitably leads to high economic and time costs. Second, RBDO faces challenges in efficiency and convergence. Such optimization typically requires nested optimization, where the outer loop optimizes design variables and the inner loop handles uncertainty analysis, relying on performance evaluation as the core. For lithium-ion batteries, performance evaluation involves coupled multi-physics analyses, including electrochemical, heat transfer, and mechanical processes. The high computational demands of multi-physics analysis, combined with the complexity of nested optimization, present significant challenges for the RBDO of lithium-ion batteries.

This study presents an RBDO approach for lithium-ion batteries considering the venting threshold, to obtain a reliable design solution that meets thermal abuse test conditions. A coupled multi-physics analytical model is developed to predict the venting threshold of lithium-ion batteries, which serves as the performance function for design optimization. Global sensitivity analysis is used to identify the key modelling parameters that influence the venting threshold, thereby reducing the complexity of the optimization process. The RBDO model is constructed with the probability of venting events occurring under thermal abuse conditions as a constraint, along with an efficient decoupling algorithm. The performance of the proposed approach is validated through engineering applications involving two prismatic lithium-ion batteries.

The remainder of this paper is organized as follows. Section II discusses the pressure evolution mechanism of lithium-ion batteries under thermal abuse conditions. Section III presents the RBDO framework and Section IV introduces the decoupling algorithm. Sections V and VI provide engineering validation and conclusions, respectively.

II. Pressure Evolution Mechanism under Thermal Abuse

A lithium-ion battery consists of a cell, casing, and tabs, as shown in Fig. 1(a). The cell features a layered structure composed of an anode, cathode, collectors, and separators. It is formed into a cylindrical or prismatic shape through winding or stacking and is then packaged in the shell. The electrolyte is injected into the cell to facilitate ionic conduction between the electrodes. During operation, it is inevitable for the battery to be exposed to high-temperature environments (e.g., exceeding 323 K), which can trigger the decomposition of the SEI on the anode surface. As shown in Fig. 1(b), the lithium carbonate in the SEI decomposes to form carbon dioxide. The lithium alkoxy compounds decompose into propane and hydrogen, and vinylene carbonate decomposes into propylene and carbon dioxide [29]. SEI regeneration occurs as a side reaction during decomposition, releasing propylene, propane, and hydrogen. Meanwhile, the decomposition and regeneration of SEI release heat, which intensifies electrochemical reactions and creates a feedback loop of heat and gas generation. This process leads to a rapid increase in internal pressure. When the pressure exceeds a certain threshold, high-temperature flammable gases may be ejected, posing significant safety risks.

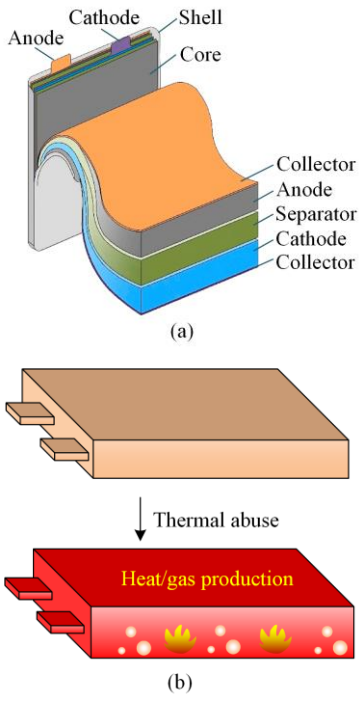

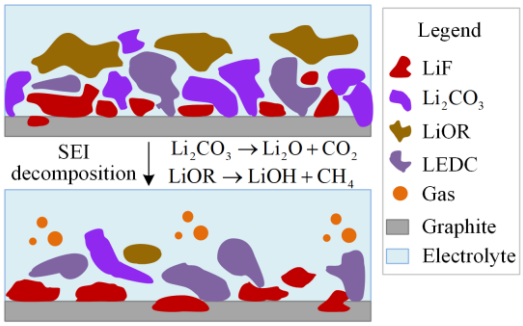

(c)

Fig. 1. The structure of lithium-ion batteries and the mechanisms of heat and gas generation under thermal abuse conditions. (a) Lithium-ion battery structure. (b) Heat/gas production. (c) SEI decomposition on the anode.

Due to the potential risk of thermal runaway in lithium-ion batteries, international organizations and government agencies have established several safety assessment standards, such as UN38.3, IEC62133, and GB/T21242 [30]. These standards require battery manufacturers to conduct mandatory testing, including thermal abuse tests [31]. This study aims to address industrial needs by conducting theoretical and experimental research based on standard test conditions. The tests involve suspending fully charged battery cells in a circulating air convection environment, heating them from 198 K to 403 K at a rate of 5 K/min, and maintaining the temperature for 30 minutes. If no venting occurs during the test, the sample is considered to have passed. To investigate the thermal behaviour of the batteries, we performed extended tests on five prismatic hard-pack battery samples, increasing the insulation time to one hour, as shown in Fig. 2(a). The test samples are in the development stage, with graphite as the anode material, lithium cobalt oxide as the cathode material, and the electrolyte mainly composed of lithium hexafluorophosphate and propylene carbonate. The shell material is 1.0 mm thick aluminum alloy, with a pressure threshold of 0.8 MPa. The venting time is monitored using a K-type thermocouple. To monitor temperature evolution, the K-type thermocouple is placed at the centre of the battery surface. The thermal abuse experiment was conducted with no external current, uniform heating rate, and forced convective airflow. The primary heat source originated from the decomposition of the SEI and its subsequent exothermic side reactions, which were uniformly distributed, resulting in minimal internal temperature gradients within the cell. The temperature at the geometric centre of the cell surface was selected to represent the overall thermal response, as single-point measurement avoids the potential interference that may arise from multipoint sensor placement.

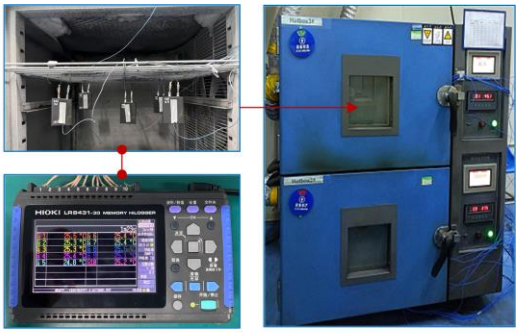

(a)

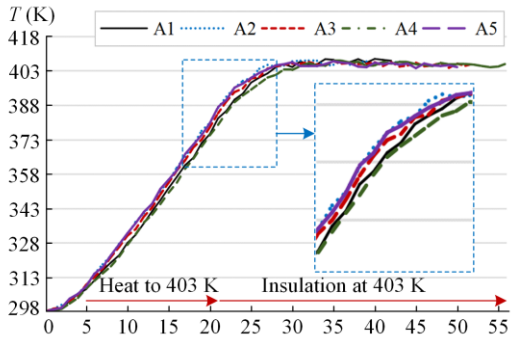

(b)

Fig. 2. The thermal abuse testing procedure and temperature evolution results of the lithium-ion battery. (a) Testing platform. (b) Experimental results.

Figure 2(b) shows the temperature evolution curves for five samples (A1–A5). These curves generally follow similar trends, though there are some differences in the details. At the end of the heating phase (1260 s), the maximum temperature difference is 7.7 K, which is 2.0% of the average value (384 K). The venting threshold times for samples A1–A5 are 2569 s, 2679 s, 3130 s, 3397 s, and 3061 s, respectively, with a maximum time difference of 828 s, representing 27.9% of the average value (2967 s). The experimental results indicate significant uncertainty in both the temperature and pressure responses of the same model battery under standard thermal abuse conditions. Notably, the venting times for samples A1 and A2 are 2569 s and 2679 s, both shorter than the specified 3060 s, meaning they did not pass the thermal abuse test. This suggests that this batch of batteries may present an unacceptable risk of thermal runaway, potentially leading to substantial economic and reputational losses. These results highlight the engineering significance of this study. Uncertainty factors cannot be ignored in the design of lithium-ion batteries. Advanced design optimization methods must be developed to achieve reliable battery designs, as uncertainty factors cannot be eliminated.

III. Reliability-Based Design Optimization

Uncertainties in structure, materials, and operating conditions lead to the uncertainty of the venting critical point under thermal abuse conditions for lithium-ion

batteries. To ensure that lithium-ion batteries in mass production pass safety tests, it is crucial to theoretically guarantee that venting events under thermal abuse conditions are rare events (less than 0.1%). This study first constructs a coupled multifield analytical model to predict the venting critical time of lithium-ion batteries, which serves as the performance function for design optimization. Second, global sensitivity analysis is conducted to clarify the impact of parameter uncertainties on the critical time, incorporating high-sensitivity parameters into the RBDO model. Lastly, based on the probability of venting events occurring under thermal abuse conditions, design variables and objectives are selected to construct the lithium-ion battery RBDO model.

A. Critical Time Prediction Model

Under thermal abuse conditions, the prediction of the venting critical time for lithium-ion batteries involves dynamic submodels of electrochemical reactions, heat transfer processes, gas states, and mechanical behaviors. By coupling these submodels through state variables, a system of ordinary differential equations is formed. Solving this system provides the venting critical time for the lithium-ion battery, serving as the performance function for design optimization. The electrochemical submodel describes the heat and gas generation during SEI decomposition and regeneration. The heat transfer submodel characterizes the heat conduction and convection between the cell and environment. The gas state equation establishes the relationship between the internal gas temperature, pressure, and volume. The mechanical submodel describes the nonlinear elastic deformation of the cell under pressure. The coupling mechanisms of these submodels are illustrated in Fig. 3.

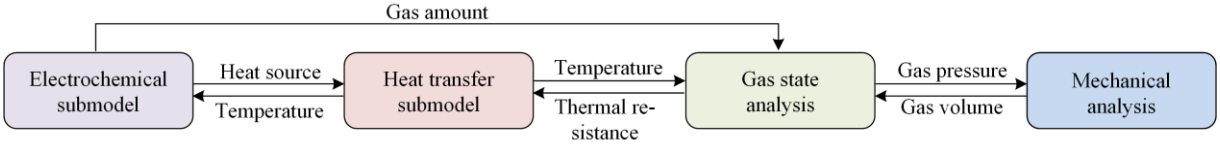

Fig. 3. The prediction of the critical venting time involves the coupling mechanisms of electrochemical, thermal, and mechanical fields.

1) Reaction Submodel

Under standard thermal abuse conditions, the heat generation in lithium-ion batteries primarily originates from the SEI decomposition and regeneration reactions on the anode [32]. The heat generation equation, proposed in [31], is widely used in battery state modelling and is expressed as:

$$Q(t) = m_{\mathrm{A}}\left(h_{\mathrm{D}}v_{\mathrm{D}}(t) + h_{\mathrm{R}}v_{\mathrm{R}}(t)\right) \tag{1}$$

where Q represents the heat generation rate; t denotes the current time; and m_{A} is the active material mass; subscripts D and R indicate SEI decomposition and regeneration reactions, respectively; while h and v represent the corresponding enthalpy change and reaction rate. The reaction rate equation is based on the classical Arrhenius formula [33] and expressed as:

$$\begin{aligned} v_{\mathrm{D}} &= -\frac{\mathrm{d}x_{\mathrm{D}}}{\mathrm{d}t} = f_{\mathrm{D}}x_{\mathrm{D}}(t)\times\exp\left(-\frac{E_{\mathrm{A}}}{R_{\mathrm{U}}T(t)}\right) \\ v_{\mathrm{R}}(t) &= -\frac{\mathrm{d}x_{\mathrm{R}}}{\mathrm{d}t} = \\ & f_{\mathrm{R}}x_{\mathrm{R}}(t)\times\exp\left(-\frac{y(t)}{y^{0}}\right)\times\exp\left(-\frac{E_{\mathrm{A}}}{R_{\mathrm{U}}T(t)}\right) \end{aligned} \tag{2}$$

where f and E_{A} represent the reaction frequency and activation energy, respectively; R_{U} is the universal gas constant, i.e., 8.314 J/(mol·K); x_{D} represents the fraction of lithium ions contained in the SEI; and x_{R} represents the fraction of lithium ions embedded in the SEI; y denotes the dimensionless SEI thickness; and y^{0} is its initial value. The increase in y corresponds to the decrease in x_{R}, written as:

$$\frac{\mathrm{d}y}{\mathrm{d}t} = -\frac{\mathrm{d}x_{\mathrm{R}}}{\mathrm{d}t} \tag{3}$$

During SEI decomposition and regeneration reactions, gas production accompanies heat generation. The gas production rate is synchronized with the reaction rate and expressed as:

$$\frac{\mathrm{d}m_{\mathrm{G}}}{\mathrm{d}t} = \gamma_{\mathrm{D}}v_{\mathrm{D}}(t) + \gamma_{\mathrm{R}}v_{\mathrm{R}}(t) \tag{4}$$

where m_{G} represents the gas production amount; and γ is the gas production coefficient corresponding to the reaction.

2) Heat Transfer Submodel

The heat transfer equation describes the conduction and convective heat transfer from the heat source within the cell to the surrounding environment. Given that the structure and operating conditions of lithium-ion batteries are symmetric in the thickness direction, the heat transfer equation is derived based on Kirchhoff's law [34], as:

$$\frac{1}{2}Q(t) = \frac{T(t) - T_{\mathrm{A}}(t)}{R_{\mathrm{G}} + R_{\mathrm{H}} + R_{\mathrm{A}}} + C\times\frac{\mathrm{d}T}{\mathrm{d}t} \tag{5}$$

where T_{A} represents the ambient temperature. For standard thermal abuse conditions, it is expressed as a piecewise function, as:

$$T_{\mathrm{A}}(t) = \begin{cases} 298 + t/12, & 0\ \mathrm{s} \leqslant t \leqslant 1260\ \mathrm{s} \\ T_{\mathrm{A}}^{\max} = 403, & t > 1260\ \mathrm{s} \end{cases} \tag{6}$$

For normalization, temperature in this study is expressed in absolute temperature units (K). RG represents the gap thermal resistance, which is related to the thermal conductivity of the gas (K_G), the heat transfer area (A), and the gap distance (δ), as:

$$R_G = \delta(t)/(K_G A) \tag{7}$$

The heat transfer area for prismatic cells is the rectangular area perpendicular to the thickness direction. For cylindrical cells, the area is the product of the circumference and height. R_A denotes the convective thermal resistance between the battery surface and the environment, which is inversely proportional to the product of the heat transfer area and the heat transfer coefficient (h_A), as:

$$R_A = 1/(h_A A) \tag{8}$$

where C represents the thermal capacity of the battery, expressed as:

$$C = cm_B \tag{9}$$

where c and m_B are the specific heat capacity and mass of the cell, respectively.

3) Gas State Submodel

The gas state equation describes the relationship between the temperature, pressure, and volume of the reaction gases. The lithium-ion battery is equipped with a pressure relief valve, with gas pressure maintained below 2.0 MPa and the gas temperature above 273 K. Under the assumption of ideal gas behaviour, the gas state equation is derived as:

$$\delta(t)AP(t)=R_C m_G(t)T(t) \tag{10}$$

where P represents the gas pressure; and R_C denotes the gas constant.

4) Mechanics Submodel

As shown in Fig. 4, the gas pressure causes compressive deformation of the battery cell. The cell is a porous composite material with nonlinear elastic mechanical characteristics [35]. The relationship between pressure and deformation is derived as:

$$P(t) - P_A = E \times \left(\frac{\delta(t) - \delta^0}{H^0} \right)^{\lambda} \tag{11}$$

where P_A represents the atmospheric pressure; and δ^0 represents the assembly gap; E and λ are the elastic modulus and strain exponent in the mechanical constitutive equation, reflecting the nonlinear elastic deformation response of the cell under pressure.

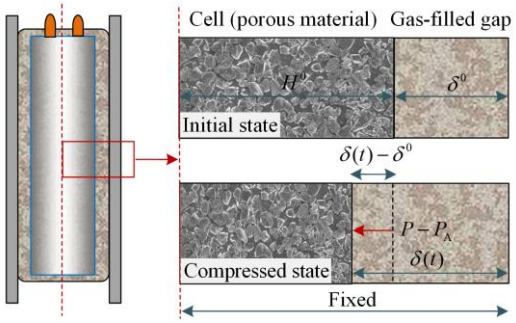

Fig. 4. The deformation of lithium-ion battery cells under gas pressure.

The integration of (1) to (11) forms a coupled multi-field analytical model, which is a system of ordinary differential equations. This system includes coupled variables such as heat generation rate (Q), gas production (m_G), temperature (T), pressure (P), and gap distance. The input parameters consist of static parameters and initial values of dynamic variables. The static variables include the mass of active material (m_A), reaction enthalpy change (h_D, h_R), reaction rate (f_D, f_R), activation energy (E_A), gas production coefficients (γ_D, γ_R), heat transfer area (A), thermal conductivity (K_G), heat transfer coefficient (h_A), specific heat capacity (c), battery cell mass (m_B), gas constant (R_C), and mechanical parameters (E, λ). The initial values of dynamic variables include lithium-ion fraction (x_D^0), embedded lithium-ion fraction (x_R^0), SEI thickness (y^0), gas production amount (m_G^0), gap distance (δ^0), and cell height (H^0). The correspondence between the coupled variables and the submodels is shown in Table I.

TABLE I
COUPLING RELATIONSHIPS BETWEEN BARIABLES AND SUBMODELS IN THE CRITICAL VENTING PREDICTION MODEL

Coupled variables	Reaction submodel	Thermal submodel	Gas state submodel	Mechanics submodel
Q	√	√		
m_G	√		√	
T	√	√	√	
P			√	√
δ			√	√

The venting critical time prediction model involves a dynamic and strongly nonlinear process. A discrete algorithm with equal time intervals decomposes the dynamic problem into a sequence of static problems over equal time steps. The state values calculated in the previous time step are used as inputs for the next step, and the state of each time step is solved sequentially. For each time step, a quasi-Newton method is applied to solve the analytical equations of the static problem [36]. The final output is the evolution curve of the gas pressure, and the critical time is determined once the pressure relief threshold is reached.

Compared with existing thermal abuse modelling approaches for lithium-ion batteries [25], [31], the proposed critical venting prediction model exhibits clear advantages in multi-physics analytical modelling and numerical solution strategies. This model integrates four submodels of electrochemical reaction, heat conduction, gas state, and mechanical response, and achieves coupling through unified state variables. It comprehensively captures the heat generation, gas production, pressure rise, and structural deformation processes induced by SEI decomposition and regeneration,

thereby enhancing the physical fidelity of thermal runaway evolution. Unlike localized models focusing solely on temperature rise or gas production, the proposed model incorporates nonlinear elastic mechanical behavior to quantify cell deformation under gas pressure and explicitly defines the venting criterion. Regarding solution strategy, the model combines equal-interval discretization with a quasi-Newton iterative scheme to overcome numerical instability caused by strong nonlinear coupling, enabling robust simulation of pressure evolution and accurate prediction of critical venting time.

B. Global Sensitivity Analysis

Based on the proposed pressure relief critical point prediction model, a given set of input parameters yields the corresponding critical moment, which can be expressed as a performance function:

$$t_{\mathrm{C}} = f(\boldsymbol{X}) \tag{12}$$

where t_{C} represents the pressure relief critical time under thermal abuse conditions; and $\boldsymbol{X}$ is the parameter vector containing 23 elements.

Collecting a large volume of sample data for each parameter to measure its uncertainty would incur significant costs. Therefore, global sensitivity analysis is employed to select modelling parameters [37], providing a theoretical foundation for selecting uncertain parameters in the RBDO. Unlike local sensitivity measures, variance-based global sensitivity analysis provides a comprehensive understanding of how parameter variability influences the output of highly nonlinear models. This method decomposes the total output variance into contributions from individual input parameters and their interactions, thereby quantifying both first-order effects and higher-order interaction effects. However, conventional variance-based global sensitivity analysis assumes statistical independence among input parameters, which limits its ability to capture potential dependencies between variables. For systems involving complex correlations, a Copula-based global sensitivity analysis framework [38] can be employed to construct joint distributions while preserving marginal characteristics, enabling a more accurate assessment of sensitivities in parameter systems with correlated structures.

In engineering applications, only a small number of samples or references are required to determine the uncertainty domain of parameters, i.e., $\boldsymbol{X}_j \in \left[\boldsymbol{X}_j^L, \boldsymbol{X}_j^R\right]$. $\boldsymbol{X}_j$ represents the jth element of $\boldsymbol{X}$, while superscripts L and R indicate the lower and upper bounds, respectively. Latin hypercube sampling is used to obtain two sets of sample matrices, $\boldsymbol{A}$ and $\boldsymbol{B}$, within the uncertainty domain of $\boldsymbol{X}$. The jth column of matrix $\boldsymbol{A}$ is replaced with the jth column of matrix $\boldsymbol{B}$ to form a combined sample matrix of $\boldsymbol{C}^{(j)}, j = 1, 2, \cdots, N$. Each matrix has a dimension of $M \times N$, where M is the number of samples, and its value range is specified as $\left[10^3, 10^5\right]$. For each sample in matrix $\boldsymbol{A}$, the critical time model is applied, and the corresponding response samples are obtained as $f(\boldsymbol{A}_i), i = 1, 2, \cdots, M$. $\boldsymbol{A}_i$ denotes the vector composed of the ith row elements of $\boldsymbol{A}$. The response samples are aggregated into a vector, expressed as $\boldsymbol{f}_{\boldsymbol{A}} = \left\{f(\boldsymbol{A}_1), f(\boldsymbol{A}_2), \cdots, f(\boldsymbol{A}_M)\right\}$. Similarly, $\boldsymbol{B}$ and $\boldsymbol{C}^{(j)}$ correspond to the response sample vectors $\boldsymbol{f}_{\boldsymbol{B}} = \left\{f(\boldsymbol{B}_1), f(\boldsymbol{B}_2), \cdots, f(\boldsymbol{B}_M)\right\}$ and $\boldsymbol{f}_{\boldsymbol{C}}^{(j)} = \left\{f\left(\boldsymbol{C}_1^{(j)}\right), f\left(\boldsymbol{C}_2^{(j)}\right), \ldots, f\left(\boldsymbol{C}_M^{(j)}\right)\right\}$.

The variance of the response samples is calculated as:

$$\boldsymbol{V}_{\mathrm{f}} = \mathrm{E}\left(f(\boldsymbol{B}_i) - \mathrm{E}(\boldsymbol{f}_{\boldsymbol{B}})\right)^2 \tag{13}$$

where $\mathrm{E}(\cdot)$ represents the operator for computing the mean value. The global sensitivity index characterizes the overall effect of an input parameter $(\boldsymbol{X}_j)$, including its main effect and interaction with other parameters, expressed as:

$$\mathrm{S}_j^{\mathrm{T}} = \frac{1}{2\boldsymbol{V}_{\mathrm{f}}} \times \mathrm{E}\left(\boldsymbol{f}_{\boldsymbol{B}} - \boldsymbol{f}_{\boldsymbol{C}}^{(j)}\right)^2 \tag{14}$$

In this study, parameter sensitivity analysis is used for sensitivity ranking rather than precise calculation of sensitivity indices. Therefore, a sample size of 10^3 is suggested to reduce computational costs. The global sensitivity analysis requires evaluating the performance function $(N+2)\times 10^3$ times. High-sensitivity parameters are selected for the RBDO, while low-sensitivity parameters are treated as constants. The parameter vector $\boldsymbol{X} = (\boldsymbol{X}_1, \boldsymbol{X}_2, \cdots, \boldsymbol{X}_N)$ is reduced to $\boldsymbol{Y} = (\boldsymbol{Y}_1, \boldsymbol{Y}_2, \cdots, \boldsymbol{Y}_L)$, $L < N$, and the performance function $f(\boldsymbol{X})$ is rewritten as $f(\boldsymbol{Y})$.

C. RBDO Model

The RBDO model for lithium-ion batteries considering the venting critical time is formulated as:

$$\begin{cases} \min\limits_{\boldsymbol{d}} \ \mathrm{obj}(\boldsymbol{d}) \\ \text{s.t. } P_{\mathrm{r}}\left(f(\boldsymbol{Y}) - t_{\mathrm{thr}}^{\mathrm{t}} \geqslant 0\right) \geqslant P_{\mathrm{r}}^{\mathrm{t}},\ \boldsymbol{d}^{\mathrm{L}} \leqslant \boldsymbol{d} \leqslant \boldsymbol{d}^{\mathrm{R}} \end{cases} \tag{15}$$

where obj represents the design objective; and $\boldsymbol{d}$ is the design vector, which is determined based on engineering requirements; $t_{\mathrm{thr}}^{\mathrm{t}}$ represents the target value for the venting critical time, i.e., $t_{\mathrm{thr}} = 3060$ s. It is the sum of the heating and holding times specified under standard thermal abuse conditions. P_{r} and $P_{\mathrm{r}}^{\mathrm{t}}$ represent the probability of the battery passing the thermal abuse test and its target value, respectively, which are also referred to as reliability and target reliability.

The proposed RBDO framework uses global sensitivity analysis to select key model parameters for predicting the venting critical time of lithium-ion batteries. This reduces the dimensionality of design variables, decreasing the RBDO complexity. However, solving the RBDO model still presents a challenge due to the nested optimization structure: the outer layer searches for the optimal design, while the inner layer evaluates probability constraints based on the critical time evaluations. Such nested optimization typically requires hundreds to thousands of calls to the performance function, resulting in high computational costs. The established performance function is an analytical model with millisecond-level computational efficiency, alleviating the computational burden of nested optimization. However, to enhance the applicability of the proposed framework for supporting time-consuming simulations as performance functions, it is necessary to develop a decoupling algorithm to improve solution efficiency.

IV. Decoupling Algorithm

The decoupling algorithm is an efficient method that transforms nested optimization into a cycle of deterministic design optimization and probability constraint assessment. In each cycle, the probability constraint is converted into an equivalent deterministic constraint, forming a deterministic optimization problem to update the design solution. The probability constraint assessment solves the reliability analysis problem, providing information for constructing the deterministic constraint in the next cycle. Sequential optimization and reliability assessment is a widely adopted decoupled algorithm in reliability-based design optimization [39], whose accuracy, computational efficiency, and convergence performance have been extensively validated in practical engineering applications [40]. The detailed procedure is outlined as follows.

A. Iteration Mechanism

In the decoupling algorithm, the link between design optimization and probability constraint assessment is the shifting vector, which drives the cycle. For the probability constraint in (15), its feasible domain boundary is denoted as $P_{\mathrm{r}}\left(f(\boldsymbol{Y})-t_{\mathrm{thr}}^{\mathrm{t}}\geqslant 0\right)=P_{\mathrm{r}}^{\mathrm{t}}$. Ignoring uncertainty, the probability constraint degenerates into a deterministic constraint, with its feasible domain boundary represented by $f(\boldsymbol{\mu}_{\boldsymbol{Y}})-t_{\mathrm{thr}}^{\mathrm{t}}=0$, and $\boldsymbol{\mu}_{\boldsymbol{Y}}$ as the mean vector of $\boldsymbol{Y}$. The feasible domain of the deterministic constraint is larger than that of the probability constraint, and the difference in their boundaries is a vector. Converting the probability constraint into a deterministic constraint involves shifting the boundary of the deterministic constraint by a vector in the feasible direction to shrink the feasible domain, approximating the feasible domain of the probability constraint, denoted as $f\left(\boldsymbol{\mu}_{\boldsymbol{Y}}-\boldsymbol{S}^{(k)}\right)-t_{\mathrm{thr}}^{\mathrm{t}}=0$. Therefore, in the kth iteration step, the optimization model is rewritten as:

$$\begin{cases}\min\limits_{\boldsymbol{d}}\ \mathrm{obj}(\boldsymbol{d})\\ \text{s.t. } f\left(\boldsymbol{\mu}_{\boldsymbol{Y}}-\boldsymbol{S}^{(k)}\right)-t_{\mathrm{thr}}^{\mathrm{t}}\geqslant 0,\ \boldsymbol{d}^{\mathrm{L}}\leqslant\boldsymbol{d}\leqslant\boldsymbol{d}^{\mathrm{R}}\end{cases}\tag{16}$$

The conventional optimization algorithms, such as the sequential quadratic programming [41], is used to solve (16) to obtain the design solution $\left(\boldsymbol{d}^{(k)}\right)$ in the current cycle.

B. Probability Constraint Assessment

The shifting vector defines the distance and direction by which the probabilistic constraint boundary is adjusted toward its equivalent deterministic boundary and is obtained via the performance measure approach for reliability assessment. In this method, the performance function value is treated as the optimization objective, while the target reliability index serves as the constraint. The algorithm searches for the point closest to the limit state within a confidence region to evaluate the probability that the system satisfies the required performance. Compared with the traditional first-order reliability method, the performance measure approach transforms the optimization variable from the Most Probable Point in the standard normal space to the performance response, thereby improving numerical stability when handling strongly nonlinear performance functions and avoiding issues such as gradient instability and iterative oscillation.

The approach maps the performance function to the standard normal space, i.e., the original space's $f(\boldsymbol{Y})$ is written as $g(\boldsymbol{U})$ in the standard normal space. $\boldsymbol{U}$ represents the vector of $\boldsymbol{Y}$ in the standard normal space, where each element in the $\boldsymbol{U}$ vector has a mean of 0 and a standard deviation of 1. The target reliability $(P_{\mathrm{r}}^{\mathrm{t}})$ is converted into the target reliability index (β^{t}), shown as:

$$\beta^{\mathrm{t}}=\Phi^{-1}(R^{\mathrm{t}})\tag{17}$$

where Φ^{-1} epresents the inverse function of the standard normal cumulative distribution. For example, a reliability of $R^{\mathrm{t}}=99.4\%$ corresponds to an index of $\beta^{\mathrm{t}}=2.5$. The performance measurement algorithm can determine the tangent point between the β^{t}-isosurface and the limit state surface, i.e., the maximum possible point. Thus, an optimization problem is formulated as:

$$\begin{cases}\min\limits_{U}\ g(\boldsymbol{U})\\ \text{s.t. } \|\boldsymbol{U}\|=\beta^{\mathrm{t}}\end{cases}\tag{18}$$

Then, the obtained maximum possible point is mapped back to the original space, i.e., $\boldsymbol{Y}^{*}$. The difference between the mean vector $\boldsymbol{\mu}_{\boldsymbol{Y}}$ of the previous

cycle and the maximum possible point in the original space forms the current shifting vector as:

$$\boldsymbol{S}^{(k)} = \boldsymbol{\mu}_{\boldsymbol{Y}}^{(k-1)} - \boldsymbol{Y}^{*(k-1)} \tag{19}$$

C. Convergence Criteria and Solution Process

The deterministic design optimization and probabilistic constraint evaluation are performed iteratively in an alternating manner until both the design vector and the probabilistic constraint converge, expressed as:

$$\begin{cases} \dfrac{\left\| \boldsymbol{d}^{(k)} - \boldsymbol{d}^{(k-1)} \right\|}{\left\| \boldsymbol{d}^{(k)} \right\|} \leqslant \varepsilon \\ f\left(\boldsymbol{\mu}_{\boldsymbol{Y}}^{(k)} - \boldsymbol{S}^{(k)} \right) - t_{\text{thr}}^{\text{t}} \geqslant 0 \end{cases} \tag{20}$$

where ε denotes the convergence tolerance, recommended to be 10^{-3}. The solution process for the proposed RBDO of lithium-ion batteries is summarized in Fig. 5.

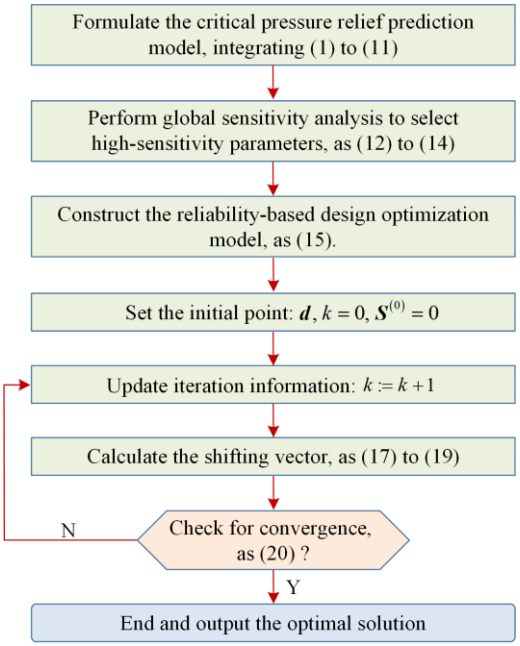

Fig. 5. The flowchart of the proposed RBDO algorithm for lithium-ion batteries.

The proposed decoupled algorithm decomposes the RBDO process into two components: deterministic design optimization and probabilistic constraint evaluation, which are executed in an iterative, alternating fashion. In each iteration, the performance measure approach is first employed to evaluate the probability that the current design solution satisfies the reliability constraint under the influence of random parameters. The most probable point is searched within the confidence region, and the corresponding reliability index is assessed. Subsequently, a shifting vector is constructed to adjust the probabilistic constraint boundary, yielding an equivalent deterministic constraint. Deterministic optimization is then performed within the updated feasible region to obtain a new design solution. This alternating procedure continues between the design space and the uncertainty space until the convergence criteria are satisfied. The algorithm avoids the high computational cost and demonstrates strong numerical stability when handling highly nonlinear performance functions.

V. Engineering Applications

Experimental and numerical results validate the performance of the proposed approach for two types of prismatic hard-pack lithium-ion batteries. The experimental conditions are based on the standard thermal abuse test, with specific details provided in Section II. The two batteries studied are designated as A-type and B-type. They have similar electrode materials, manufacturing processes, and experimental conditions. The relevant modelling parameters are summarized in Table II. The two battery types share similar characteristics and their cell properties differ with corresponding parameters in Table III. The parameter information in Tables II and III includes nominal values and fluctuation ranges. The data is sourced from our previous research [42]. To verify the randomness of the battery state response, five samples of the same model were tested simultaneously. The sample numbers for the two battery types are A1–A5 and B1–B5.

TABLE II
THARED MODELLING PARAMETERS OF THE TWO LITHIUM-ION BATTERY SAMPLES

Character	Unit	Nominal value	Fluctuation range	Character	Unit	Nominal value	Fluctuation range
h_{D}	J/g	257	254.4, 259.6	c	J/(g·K)	0.95	0.94, 0.96
h_{R}	J/g	1714	1697, 1731	R_{C}	J/(g·K)	0.21	0.20, 0.22
f_{D}		1.67×10^{15}	1.65×10^{15}, 1.69×10^{15}	E	MPa	3.634	3.600, 3.668
f_{R}		2.50×10^{13}	2.48×10^{13}, 2.53×10^{13}	λ		3.473	3.438, 3.508
E_{A}	J/mol	1.35×10^{5}	1.34×10^{5}, 1.36×10^{5}	x_{D}^{0}		0.15	0.14, 0.16
γ_{D}	g	0.156	0.154, 0.158	x_{R}^{0}		0.75	0.74, 0.76
γ_{R}	g	0.142	0.141, 0.143	y^{0}		0.97	0.96, 0.98
K_{G}	W/(mm·K)	0.236	0.212, 0.260	δ^{0}	mm	0.25	0.20, 0.30
h_{A}	W·mm^2/K	3.0×10^{-5}	2.5×10^{-5}, 3.5×10^{-5}	P_{thr}	MPa	0.80	0.79, 0.81

TABLE III
DISTINCT MODELLING PARAMETERS OF THE TWO LITHIUM-ION BATTERY SAMPLES

Character	Unit	A-type		B-type	
		Nominal value	Fluctuation range	Nominal value	Fluctuation range
A	mm^2	4408	4406, 4410	5642	5640, 5644
H^0	mm	5.8	5.7, 5.9	4.8	4.7, 4.9
m_A	g	16.0	15.8, 16.2	16.6	16.4, 16.8
m_B	g	34.1	33.8, 34.4	35.3	34.9, 35.7

A. Validation of the Critical Time Prediction Model

The critical time prediction model is applied to solve the temperature evolution and venting critical times for two battery types. Given the pressure relief threshold ($P_{thr} = 0.8$ MPa) and time step interval ($\tau = 5$ s), the solution times for the two processes are 5 s and 6 s, respectively. The average experimental and predicted temperature curves for both batteries are shown in Fig. 6. The experimental results for each sample of two battery types are shown in Fig. 7. The experimental and predicted critical times for samples are listed in Table IV.

TABLE IV
COMPARISON OF EXPERIMENTAL AND PREDICTED CRITICAL VENTING TIMES FOR TWO BATTERIES UNDER THERMAL ABUSE CONDITIONS

Critical time	A-type						B-type					
	A1	A2	A3	A4	A5	Mean value	B1	B2	B3	B4	B5	Mean value
Experimental value (s)	2569	2679	3130	3397	3061	**2967**	4133	4289	3690	3791	4450	**4071**
Predicted value (s)	2980	2980	2980	2980	2980	**2980**	3985	3985	3985	3985	3985	**3985**
Related error (%)	16.0	11.2	−4.8	−12.3	−2.6	**0.4**	−3.6	−7.1	8.0	5.1	−10.4	**−2.1**

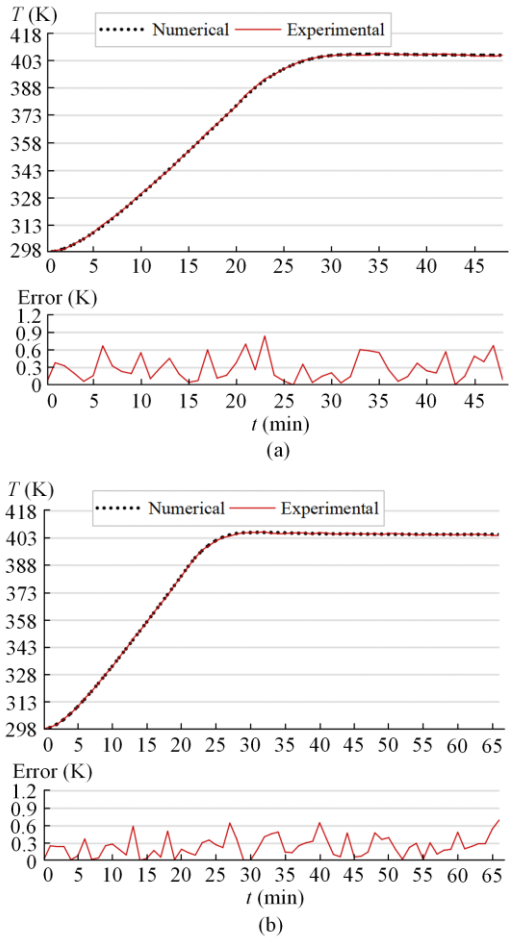

Fig. 6. Comparison of experimental mean temperatures and predicted temperature curves for two batteries under thermal abuse conditions. (a) Sample_A. (b) Sample_B.

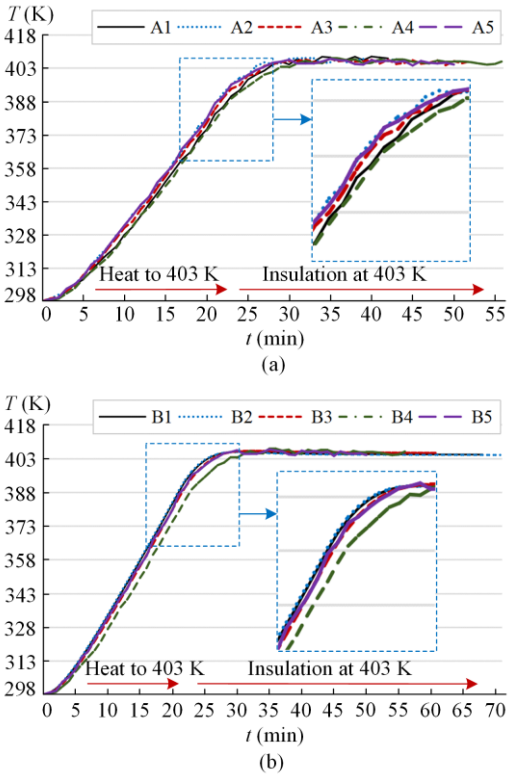

Fig. 7. Uncertainty in temperature responses of battery samples under thermal abuse conditions. (a) Sample_A. (b) Sample_B.

Figure 6 illustrates the comparison between experimental mean temperature curves and model predictions for the two types of batteries (Sample_A and Sample_B) under thermal abuse conditions. Throughout the heating and holding phases, the predicted temperature profiles align closely with the experimental means, particularly

near the thermal inflection point (~403 K), where the fitting accuracy is notably high. The corresponding error curves show that the maximum temperature deviation remains below 1 K, with peak discrepancies of 0.83 K for Sample_A and 0.72 K for Sample_B, and root mean square errors (RMSE) of 0.22 K and 0.18 K, respectively. These results confirm that the proposed multi-physics analytical model demonstrates strong predictive accuracy and numerical stability in capturing temperature evolution.

As shown in Fig. 7, the individual temperature response curves exhibit significant sample-to-sample variability. Under identical thermal abuse conditions, cells of the same type display measurable divergence and fluctuation in thermal behavior. This variability is particularly evident in two distinct stages. During the heating phase (0–403 K), certain samples (e.g., A4 and B1) exhibit slightly faster temperature rise, likely due to subtle differences in local thermal conductivity or resistance. In the holding phase (at 403 K), samples reach the temperature plateau at different times, with noticeable variations in the slope of their temperature curves. These differences reflect inter-sample variability in heat capacity and reaction kinetics, thereby highlighting the necessity of incorporating parameter uncertainties in the design optimization process.

Moreover, the proposed critical venting prediction model demonstrates consistent trend-capturing capability across different samples. As shown in Table V, although the experimentally observed venting times exhibit significant dispersion (with a maximum deviation of 828 s), the model-predicted mean values closely match the experimental averages, with relative errors of only 0.4% for Sample_A and −2.1% for Sample_B. This consistency highlights the model's robust ability to capture the gas generation induced pressure evolution and to accurately predict the critical venting time of lithium-ion batteries under thermal abuse.

TABLE V
VERIFICATION OF SOLUTION CONSISTENCY IN STATE EVOLUTION FOR TWO BATTERY TYPES

Evaluation metric	Sample_A	Sample_B
Maximum temperature error (K)	0.83	0.72
Root mean square error (RMSE, K)	0.22	0.18
Deviation in critical venting time	0.4% (13 s)	−2.1% (86 s)
Max deviation among 5 samples (s)	828 (A1 vs A4)	760 (B3 vs B5)
Single prediction runtime (s)	5	6

To further validate the effectiveness of the proposed model, comparative evaluations are conducted against representative electrochemical-thermal coupled simulation models and conventional analytical models [43], [44]. These comparisons are made across three key dimensions: physical modelling completeness, prediction accuracy, and computational efficiency. High-fidelity simulation models, based on finite element methods, offer detailed characterization of multi-physics interactions and achieve high predictive accuracy. However, they incur substantial computational costs, with single-run solutions typically requiring several minutes to hours. In contrast, conventional analytical models feature superior computational speed but often lack a comprehensive coupling of heat generation, gas production, pressure rise, and structural deformation, thereby limiting their physical representativeness. The proposed analytical model addresses these limitations by integrating electrochemical kinetics, heat conduction, gas dynamics, and nonlinear mechanics into a unified multi-physics framework. It achieves second-level computational efficiency while maintaining high fidelity in predicting both temperature evolution and critical venting time. This balanced performance across accuracy, efficiency, and physical realism underscores its superiority in practical engineering applications.

B. Global Sensitivity Analysis

Based on the critical time prediction model and the fluctuation ranges of the modelling parameters, global uncertainty measurement is performed on the parameters to provide a basis for selecting uncertain parameters in RBDO. The number of samples is set to 10^3. The time for solving parameter sensitivity for two battery types is 34.7 hours and 41.7 hours, respectively. Table VI lists the modelling parameters with high-sensitivity, with their indices greater than 0.01. The sensitivity index rankings for both battery types are similar. The high-sensitivity parameters include: activation energy (E_A), assembly gap (δ^0), gas constant (R_C), cutoff temperature (T_A^{max}), strain index (λ), and pressure threshold (P_{thr}). Among them, activation energy has the highest global sensitivity index.

TABLE VI
GLOBAL SENSITIVITY ANALYSIS RESULTS OF MODEL PARAMETERS UNDER THERMAL ABUSE CONDITIONS FOR CRITICAL VENTING PREDICTION.

Parameter	E_A	δ^0	R_C	T_A^{max}	λ	P_{thr}
A-type	0.585	0.255	0.204	0.092	0.020	0.019
B-type	0.832	0.231	0.132	0.096	0.015	0.013

Within their respective variation ranges, high-sensitivity parameters exert significant influence on the prediction of the critical venting time. The activation energy governs the temperature dependence of the reaction rate; an increase in its value suppresses the SEI decomposition process, thereby delaying gas generation and heat accumulation, ultimately postponing the venting onset. As a structural parameter, assembly gap reflects manufacturing tolerances; a larger gap increases the available expansion volume, reduces the pressure rise rate, and delays the triggering moment.

Variations in the gas constant stem from uncertainties in gas composition and affect pressure estimation per unit gas generation, thereby influencing critical time prediction. Deviations in cut-off temperature result from thermal control uncertainty in abuse testing; even slight increases in the upper bound significantly accelerate reaction kinetics and pressure buildup. The strain index characterizes the nonlinear compressive behavior of the battery core; a higher index indicates limited deformation capability, promoting gas accumulation in a smaller volume and accelerating the onset of critical conditions. The pressure threshold, as the venting trigger criterion, has a direct linear effect on the predicted critical time, with its variation determining the decision boundary of the model.

High-sensitivity parameters are modeled as normally distributed random variables in the subsequent optimization process, while low-sensitivity parameters are treated using their nominal values to reduce computational dimensionality. It is important to note that although several parameters exhibit high-sensitivity indices in the global sensitivity analysis, not all possess engineering tunability for use as design variables. Activation energy and strain index are intrinsic material properties that typically remain constant once the material system is determined, making them unsuitable for adjustment during structural design. The gas constant is a fixed physical property of the reaction gases and cannot be artificially modified. The cut-off temperature, as a boundary condition in thermal abuse testing, is constrained by regulatory standards and cannot be freely adjusted. The pressure threshold is governed by battery structural design codes and safety regulations, allowing only limited tuning. Therefore, this study selects the assembly gap as the design variable due to its clear adjustability in battery structural configuration. It directly influences gas accumulation, pressure evolution, and the mechanical response of the battery core, serving as a crucial link between structural design and reliability objectives. This highlights the practical feasibility and engineering relevance of the proposed method.

C. RBDO Solution

The global sensitivity measure indicates that the assembly gap has the greatest impact on the venting criticality of lithium batteries under thermal abuse conditions. A large assembly gap may lead to sliding friction between the battery cell and the shell, causing structural damage and potentially triggering a short circuit. Conversely, a small gap may result in the venting criticality occurring before the thermal abuse test ends, thus failing to meet safety standards. In response to engineering requirements, the nominal value of the assembly gap is set as a design variable and objective, while the probability of exceeding the target reliability in thermal abuse tests is treated as a constraint. The RBDO is formulated as:

$$\begin{cases} \min\limits_{\mu_\delta} \ \mu_\delta \\ \text{s.t. } P_r\left(f(E_A,\delta^0,R_C,T_A^{\max},\lambda,P_{thr})-t_{thr}^t \geqslant 0\right) \geqslant \\ \quad P_r^t = 99.4\%,\ 0.1\ \text{mm} \leqslant \mu_\delta \leqslant 1.0\ \text{mm} \end{cases} \tag{21}$$

where μ_δ represents the nominal value (δ^0) of the assembly gap. Samples of high-sensitivity parameters (E_A, δ^0, R_C, $T_A^{\max}$, λ, P_{thr}) are collected and treated as normal random variables. Their mean values and standard deviations are listed in Table VII.

TABLE VII
THE UNCERTAINTY QUANTIFICATION OF HIGHLY SENSITIVE PARAMETERS IN THE VENTING THRESHOLD PREDICTION MODEL

Parameter	E_A	δ^0	R_C	$T_A^{\max}$	λ	P_{thr}
Unit	J/mol	mm	J/(g·K)	K		MPa
Mean value	1.35×10^5	μ_δ	0.21	403	3.473	0.80
Standard deviation	580	0.03	0.006	1.2	0.02	0.006

Using $\mu_\delta^{(0)} = 0.25$ mm as the initial design, the decoupling algorithm is applied to solve (21). For both battery types, the solution achieves robust convergence after several iterations. The iteration solutions and optimal solutions are listed in Table VIII. The optimization process for the two types involves 972 and 1221 calls to the critical time prediction model, with computational times of 1.4 and 1.9 hours, respectively. At the initial designs of $\delta_A^0 = \delta_B^0 = 0.25$ mm, the reliability of the two types passing the thermal abuse test (43.2% and 62.7%) is much lower than the target reliability (99.4%), indicating an unacceptable risk of thermal runaway. The optimal solutions for both types, $\delta_A^0 = 0.43$ mm and $\delta_B^0 = 0.32$ mm, are obtained using the proposed approach. At the optimal solution, the reliability for passing the thermal abuse test is 99.39% and 99.40%, slightly exceeding the target reliability. Thus, the optimal solutions are feasible.

TABLE VIII
THE RBDO SOLUTIONS CONSIDERING CRITICAL VENTING IN LITHIUM-ION BATTERIES FOR TWO SAMPLES

Type	Iteration (k)	1	2	3	4	5	6	7	8
A	Solution (mm)	0.250	0.271	0.379	0.418	0.441	0.433	0.433	
	Reliability (%)	43.1	56.5	95.7	98.2	99.8	99.4	99.4	
B	Solution (mm)	0.250	0.181	0.288	0.302	0.308	0.321	0.314	0.314
	Reliability (%)	92.2	52.8	97.9	98.9	99.1	99.9	99.4	99.4

D. Discussion

The performance of the proposed approach is discussed in terms of accuracy, applicability, and efficiency. RBDO involves an outer layer for searching the optimal design and an inner layer for evaluating the reliability of passing the thermal abuse test. Both layers are driven by the venting critical time prediction for lithium-ion batteries. The accuracy and efficiency of the prediction model theoretically determine the overall RBDO performance. Experimental results for five samples of each battery type show that the maximum temperature error between the experimental and predicted values is 0.83 K for the A-type and 0.72 K for the B-type. The relative errors between the predicted and experimental critical times are 0.4% for the A-type and 2.1% for the B-type. Regarding efficiency, the critical time prediction takes five seconds for A-type and six seconds for B-type. This level of accuracy and efficiency provides a solid foundation for subsequent RBDO.

In terms of applicability, global sensitivity analysis is used to identify the impact of parameter uncertainty on the fluctuation of the venting critical time. This analysis explores the range of parameter variations and identified high-sensitivity parameters such as activation energy, assembly gap, gas constant, cutoff temperature, strain index, and pressure threshold. This reduces the dimensionality of RBDO, helping lower the cost of sampling uncertain parameters and reducing its computational burden. The RBDO solving process for two battery types involves 972 and 1,221 calls to the critical time predictions, respectively, with a total computation time of less than two hours. This computational cost is acceptable for engineering applications. Reliability analysis showed that the initial designs for both batteries led to a reliability lower than the target, posing an unacceptable thermal runaway risk. Through RBDO, the solutions achieves a reliability slightly higher than the target, making them viable designs for lithium-ion batteries. In short, the proposed approach demonstrates clear advantages in accuracy, applicability, and efficiency, highlighting its strong engineering practicality.

VI. Conclusion

The state evolution of lithium-ion batteries is influenced by multiple sources of uncertainty, potentially leading to thermal runaway risks. To address this challenge, this study proposes an RBDO method incorporating critical venting prediction, aiming to derive reliable design solutions that satisfy thermal abuse testing requirements. The methodological innovations of this study can be summarized as follows. First, a physics-based analytical model is developed by coupling electrochemical reactions, heat transfer, gas dynamics, and nonlinear mechanical responses, which captures the heat/gas/mechanical evolution process induced by SEI decomposition under thermal abuse. The predicted critical venting time is incorporated as the performance metric in the design framework. Second, a global sensitivity analysis based on variance decomposition is conducted to identify key uncertain parameters affecting the venting response, enabling effective dimensionality reduction of the high-dimensional optimization problem. Finally, an RBDO model is formulated with the probability of venting as the core constraint. The model is efficiently solved using the performance measure approach and a decoupled iterative strategy, ensuring numerical convergence and computational efficiency.

Numerical and experimental results for two types of battery samples demonstrate the excellent accuracy and efficiency of the proposed method. Regarding accuracy, the maximum temperature prediction error is less than 1 K, and the relative error in critical venting time prediction is below 3%. Regarding efficiency, the RBDO model for both battery cases is solved within 2 hours, and the obtained design solutions exceed the target reliability level for passing the thermal abuse test. These results highlight the computational feasibility and practical engineering applicability of the proposed approach. In future work, we aim to extend this framework to a full life-cycle reliability-based design optimization method for lithium-ion batteries, addressing the challenges associated with modelling and solving optimization problems under stochastic processes. This will involve introducing battery aging models and lifetime prediction mechanisms, constructing time-varying functions for key parameters that evolve with cycling, and embedding them into the multi-physics modelling framework to enhance adaptability over the battery life span. A Bayesian-update-based uncertainty propagation framework will be developed to characterize the effects of manufacturing deviations and operating condition variability on performance evolution. Combined with stage-wise RBDO strategies and efficient optimization algorithms, the proposed extension will enable reliability control and performance enhancement across different aging stages.

Acknowledgment

Not applicable.

Authors' Contributions

Tongguang Yang: project administration, supervision, writing-review, and editing. Andong Ni: conceptualization, investigation, validation, and visualization. Zhiliang Huang: conceptualization, data curation, formal analysis, and writing. Hangyang Li: software, validation, and visualization. Huaixing Wang: resource, validation, and visualization. Wanyi Tian: resource, data curation, and visualization. Shouhua Yi: resource,

data curation, and visualization. All authors read and approved the final manuscript.

FUNDING

This work is supported by the National Natural Science Foundation of China (No. 52377181 and No. 52575282); the Natural Science Foundation of Hunan Province of China (No. 2025JJ50272 and No. 2025JJ70387); and Projects of Scientific Research of Hunan Provincial Department of Education (No. 24B0731).

AVAILABILITY OF DATA AND MATERIALS

Please contact the corresponding author for data material request.

DECLARATIONS

Competing interests: The authors declare that they have no known competing financial interests or personal relationships that could have appeared to influence the work reported in this article.

AUTHORS' INFORMATION

Tongguang Yang received the M.S., and Ph.D. degrees in control science and engineering from Central South University in 2008 and 2013, respectively. He is currently a professor at the School of Mechanical and Electrical Engineering, Hunan City University. His research interests include the power industry, automation technology and computer software and computer applications.

Andong Ni received the B.S. degree in electrical engineering in 2023, is currently pursuing a M.S. degree in energy and power at the School of Electrical Engineering, University of South China. His research interests include lithium-ion battery safety management.

Zhiliang Huang received the Ph.D. degree in mechanical engineering from Hunan University in 2017. He is currently a professor at the School of Mechanical and Electrical Engineering, Hunan City University. His research interests include multiphysics coupling modelling, mechanical and electrical equipment reliability analysis, and structural optimization design.

Hangyang Li received the Ph.D. degree in mechanical engineering from Hunan University in 2020. He is currently a teacher at the School of Mechanical and Electrical Engineering, Hunan City University. His research interests include optimization control theory and lithium-ion battery safety management analysis.

Huaixing Wang received the M.S. degree in mechanical engineering from Hunan University in 2022, is currently a researcher at Guangdong Province Huizhou Liwinon New Energy Technology Co., Ltd. Long-term engaged in energy storage lithium-ion battery safety management technology research and management.

Wanyi Tian received the Ph.D. degree in thermal engineering from Central South University in 2015. He joined Hunan University in 2016 and is currently an associate professor and winner of Hunan Jie qing Project. His research interests include industrial general technology and equipment, environmental science and resource utilization, and temperature field studies.

Shouhua Yi received the Ph.D. degree in mechanical engineering from Central South University in 2022. He joined Hunan University in 2010 and is currently a senior experimentalist. His research interests include lithium-ion battery research, industrial general technology and equipment, and metal processes.

REFERENCES

[1] H. Liu, L. Zhang, and L. Li, "Progress on the fault diagnosis approach for lithium-ion battery systems: advances, challenges, and prospects," *Protection and Control of Modern Power Systems*, vol. 9, no. 5, pp. 16-41, Sept. 2024.

[2] Y. Pan, J. Song, and K. Wang, "Research progress and prospects of liquid-liquid triboelectric nanogenerators: mechanisms, applications, and future challenges," *ACS Applied Electronic Materials*, vol. 7, no. 1, pp. 1-12, Dec. 2024.

[3] B. Xu, J. Lee, and D. Kwon *et al*., "Mitigation strategies for Li-ion battery thermal runaway: a review," *Renewable and Sustainable Energy Reviews*, vol. 150, Oct. 2021.

[4] Y. S. Duh, Y. Sun, and X. Lin *et al*., "Characterization on thermal runaway of commercial 18650 lithium-ion batteries used in electric vehicles: a review," *Journal of Energy Storage*, vol. 41, Sept. 2021.

[5] U. S. Meda, L. Lal, and M. Sushantha *et al*., "Solid electrolyte interphase (SEI), a boon or a bane for lithium batteries: a review on the recent advances," *Journal of Energy Storage*, vol. 47, Mar 2022.

[6] R. Peng, D. Kong, and P. Ping *et al*., "Thermal runaway modelling of lithium-ion batteries at different scales: recent advances and perspectives," *Energy Storage Materials*, vol. 69, May 2024.

[7] P. Sun, R. Bisschop, and H. Niu *et al*., "A review of battery fires in electric vehicles," Fire Technology, vol. 56, no. 4, pp. 1361-1410, Jan. 2020.

[8] R. Zalosh, P. Gandhi, and A. Barowy, "Lithium-ion energy storage battery explosion incidents," *Journal of Loss Prevention in the Process Industries*, vol. 72, Sept. 2021.

[9] A. García, J. Monsalve-Serrano, and J. M. Gimeno *et al*., "Experimental measurement and modelling of the internal pressure in cylindrical lithium-ion battery cells

under abuse conditions," *Journal of Energy Storage*, vol. 103, Dec. 2024.

[10] A. G. Olabi, H. M. Maghrabie, and O. H. K. Adhari *et al*., "Battery thermal management systems: recent progress and challenges," *International Journal of Thermofluids*, vol. 15, Aug. 2022.

[11] W. Vermeer, G. R. C. Mouli, and P. Bauer, "A comprehensive review on the characteristics and modelling of lithium-ion battery aging," *IEEE Transactions on Transportation Electrification*, vol. 8, no. 2, pp. 2205-2232, Jun. 2021.

[12] D. C. Lee and C. W. Kim, "Two-way nonlinear mechanical-electrochemical-thermal coupled analysis method to predict thermal runaway of lithium-ion battery cells caused by quasi-static indentation," *Journal of Power Sources*, vol. 475, Nov. 2020.

[13] G. Wang, D. Kong, and P. Ping *et al*., "Modelling venting behavior of lithium-ion batteries during thermal runaway propagation by coupling CFD and thermal resistance network," *Applied Energy*, vol. 334, Mar. 2023.

[14] P. Zhang, J. Lu, and K. Yang *et al*., "A 3D simulation model of thermal runaway in li-ion batteries coupled particles ejection and jet flow," *Journal of Power Sources*, vol. 580, Oct. 2023.

[15] R. Xiong, S. Wang, and P. Takyi-Aninakwa *et al*., "Critical review on improved electrochemical impedance spectroscopy-cuckoo search-elman neural network modelling methods for whole-life-cycle health state estimation of lithium-ion battery energy storage systems," *Protection and Control of Modern Power Systems*, vol. 9, no. 2, pp. 75-100, Mar. 2024.

[16] Y. Pan, Y. Hua, and S. Zhou *et al*., "A computational multi-node electro-thermal model for large prismatic lithium-ion batteries," *Journal of Power Sources*, vol. 459, May 2020.

[17] C. He, Q. Yue, and Q. Chen *et al*., "Modelling thermal runaway of lithium-ion batteries with a venting process," *Applied Energy*, vol. 327, Dec. 2022.

[18] Z. Huang, H. Wang, and W. Zou *et al*., "An online evaluation model for mechanical/thermal states in prismatic lithium-ion batteries under fast charging/discharging," *Energy*, vol. 302, Sept. 2024.

[19] Z. Yi, S. Wang, and Z. Li *et al*., "A novel approach for state of health estimation and remaining useful life prediction of supercapacitors using an improved honey badger algorithm assisted hybrid neural network," *Protection and Control of Modern Power Systems*, vol. 9, no. 6, pp. 1-18, Nov. 2024.

[20] Q. Xing, M. Zhang, and Y. Fu *et al*., "Transfer learning to estimate lithium-ion battery state of health with electrochemical impedance spectroscopy," J*ournal of Energy Storage*, vol. 110, Feb. 2025.

[21] H. Fayaz, A. Afzal, and A. D. M. Samee *et al*., "Optimization of thermal and structural design in lithium-ion batteries to obtain energy efficient battery thermal management system (BTMS): a critical review," *Archives of Computational Methods in Engineering*, vol. 29, no. 1, pp. 129-194, Jan. 2022.

[22] Y. Liu, S. Tang, and L. Li *et al*., "Simulation and parameter identification based on electrochemical-thermal coupling model of power lithium ion-battery," *Journal of Alloys and Compounds*, vol. 844, Dec. 2020.

[23] S. Li, N. Kirkaldy, and C. Zhang *et al*., "Optimal cell tab design and cooling strategy for cylindrical lithium-ion batteries," *Journal of Power Sources*, vol. 492, Apr. 2021.

[24] Z. Sun, Y. Guo, and C. Zhang *et al*., "Algorithm-driven optimization of lithium-ion battery thermal modelling," *Journal of Energy Storage*, vol. 65, Aug. 2023.

[25] Q. Xia, Y. Ren, and Z. Wang *et al*., "Safety risk assessment method for thermal abuse of lithium-ion battery pack based on multiphysics simulation and improved bisection method," *Energy*, vol. 264, Feb. 2023.

[26] H. Li, Z. Huang, and T. Yang *et al*., "Robust optimization of prismatic lithium-ion cells for reducing thermal performance fluctuations and manufacturing costs," *Journal of Energy Storage*, vol. 72, Nov. 2023.

[27] M. Yang, D. Zhang, and X. Han, "New efficient and robust method for structural reliability analysis and its application in reliability-based design optimization," *Computer Methods in Applied Mechanics and Engineering*, vol. 366, Jul. 2020.

[28] Z. Meng, G. Li, and X. Wang *et al*., "A comparative study of metaheuristic algorithms for reliability-based design optimization problems," *Archives of Computational Methods in Engineering*, vol. 28, pp. 1853-1869, May 2021.

[29] Z. Huang, H. Wang, and H. Li *et al*., "Identification of temperature-dependent gas production rates in pouch lithium-ion cells," *Applied Energy*, vol. 377, Jan. 2025.

[30] S. Gao, X. Feng, and L. Lu *et al*., "Thermal runaway propagation assessment of different battery pack designs using the TF5 draft as framework," *Journal of The Electrochemical Society*, vol. 166, no. 8, May 2019.

[31] J. K. Ostanek, W. Li, and P. P. Mukherjee *et al*., "Simulating onset and evolution of thermal runaway in li-ion cells using a coupled thermal and venting model," *Applied Energy*, vol. 268, Jun. 2020.

[32] P. Liu, L. Yang, and B. Xiao *et al*., "Revealing lithium battery gas generation for safer practical applications," *Advanced Functional Materials*, vol. 32, no. 47, Nov. 2022.

[33] D. G. Moye, P. L. Moss, and X. Chen *et al*., "Observations on arrhenius degradation of lithium-ion capacitors," *Materials Sciences and Applications*, vol. 11, no. 7, pp. 450-461, Jul. 2020.

[34] R. Drummond, L. D. Couto, and D. Zhang, "Resolving Kirchhoff's laws for parallel li-ion battery pack state-estimators," *IEEE Transactions on Control Systems Technology*, vol. 30, no. 5, pp. 2220-2227, Sept. 2022.

[35] Y. Qiu, B. Chen, and C. Chen *et al*., "Quasi-static constitutive modelling of lithium-ion battery materials under compression," *Energy Storage Science and Technology*, vol. 13, no. 10, pp. 3518-3522, Oct. 2024.

[36] M. M. A. Anjarani and N. Raharya, "An implementation of quasi-newton algorithm for fast-charging lithium-ion battery (LIB) optimization in electric vehicle application," *International Journal of Electrical, Computer, and Biomedical Engineering*, vol. 2, no. 2, pp. 218-228, Jun. 2024.

[37] E. Borgonovo and E. Plischke, "Sensitivity analysis: a review of recent advances," *European Journal of Operational Research*, vol. 248, no. 3, pp. 869-887, Feb. 2016.

[38] H. Liu, M. P. Clark, and S. Gharari *et al*., "An improved copula-based framework for efficient global sensitivity analysis," *Water Resources Research*, vol. 60, no. 1, Jan. 2024.

[39] S. S. Afshari, F. Enayatollahi, and X. Xu *et al*., "Machine learning-based methods in structural reliability analysis: a review," *Reliability Engineering & System Safety*, vol. 219, Mar. 2022.

[40] W. Hu, S. Cheng, and J. Yan *et al*., "Reliability-based design optimization: a state-of-the-art review of its methodologies, applications, and challenges," *Structural and Multidisciplinary Optimization*, vol. 67, no. 9, Oct. 2024.

[41] L. Hong, X. Yu, and G. Tao *et al*., "A sequential quadratic programming based strategy for particle swarmoptimization on single-objective numerical optimization," *Complex & Intelligent Systems*, vol. 10, no. 2, pp. 2421-2443, Apr. 2024.

[42] Z. Hu, R. Mansour, and M. Olsson *et al*., "Second-order reliability methods: a review and comparative study," *Structural and Multidisciplinary Optimization*, vol. 64, pp. 3233-3263, Dec. 2021.

[43] R. Peng, D. Kong, and P. Ping *et al*., "Thermal runaway modelling of lithium-ion batteries at different scales: recent advances and perspectives," *Energy Storage Materials*, vol. 69, May 2024.

[44] M. Alkhedher, A. B. A. Tahhan, and J. Yousaf *et al*., "Electrochemical and thermal modelling of lithium-ion batteries: a review of coupled approaches for improved thermal performance and safety lithium-ion batteries," *Journal of Energy Storage*, vol. 86, May 2024.